Corrosion Science 208 (2022) 110673

Contents lists available at ScienceDirect

Corrosion Science

journal homepage: www.elsevier.com/locate/corsci

Corrosion study of Ni-based alloy in ternary chloride salt for thermal storage application

Mickaël Lambrecht *, Gustavo García-Martín, María Teresa de Miguel, María Isabel Lasanta, Francisco Javier Pérez

Surface Engineering and Nanostructured Materials Research Group, Complutense University of Madrid, Complutense Avenue s/n, Madrid, Spain

ARTICLE INFO

Keywords:
Molten chlorides corrosion
Thermodynamic simulations
Concentrated solar power
Thermal storage

ABSTRACT

$MgCl_2$/NaCl/KCl salt appeared as a high-potential heat transfer fluid for concentrated solar application, offering a wide operating range and low cost. Nevertheless, $MgCl_2$ hydrates and atmosphere relative humidity are the limiting factors for a real scale CSP plant, leading to severe corrosion. Thus, Inconel 617 was tested at 700ºC up to 24 h in air atmosphere to simulate a punctual failure in the inertization system of a plant. XRD and SEM-EDX analysis showed unstable multilayers growing in cascade, highlighting chromium, aluminum, magnesium, and oxygen activities. Additionally, A radial growth of $MgCr_2O_4$ at the expense of MgO grains was visualized.

1. Introduction

Concentrated solar power (CSP) plants have become a solution to overcome the issues of renewable energy production worldwide. Moreover, new thermal energy storage (TES) mediums are strongly investigated to flatten the production rate of electricity over time. Indeed, molten salts as heat transfer fluids attract the attention and particularly molten chlorides, as they already show excellent thermo-physical properties. Furthermore, ternary $MgCl_2$/NaCl/KCl (53.9/24.3/21.8 wt%) provides a wide stability range [380ºC;750ºC] and low cost (0.35$/kg), making it a high potential salt for a next generation of CSP plants. Recent publications by Ding et. al suggested a new composition of at this mixture 47.1/30.2/22.7 mol.% respectively, according to its operating range of 420ºC-800ºC [1,2]. This mixture is particularly suitable for central tower technology as it could increase its receiver temperature above 700ºC leading to higher electricity production. However, the hygroscopicity of $MgCl_2$ leads to hexahydrate $MgCl_2$0.6 H_2O when exposed to air and produces corrosive MgOHCl at high temperature [3]. Humidity has been previously identified as the compound that accelerates the most the corrosivity of MgCl2-based chlorides. A small amount of water adsorbed on them leads to the harsh corrosion of materials in contact [4,5]. Therefore, humidity in salt's environment must be controlled and mitigated with the inertization of the atmosphere. Indeed, ternary MgNaK chloride mixtures have already been tested against several alloys. SS310, In800H and Ha C-276 were studied under MgCl2/NaCl/KCl (60/20/20 mol%) at 700ºC with inert argon atmosphere up to 500 h [6]. Among them, C-276 showed the best corrosion resistance with a corrosion rate of 79 μm/year. GH3535 was studied under molten and vapor MgCl2/NaCl/KCl (54.95/20.55/24.50 wt%) at 700ºC with argon atmosphere up to 100 h [7]. The results highlighted the need to mitigate chromium depletion that causes dangerous behaviors with its dissolution into the salt. 316 stainless steel was investigated with the same chloride composition in vapor, up to 95 h [8]. Authors concluded that iron and chromium were corroded preferentially, forming multilayers of oxides, with a predominance of magnesium-chromium layer. Finally, the effect of the grain size of Inconel 625 was studied under $MgCl_2$ – NaCl – KCl (53.9/24.3/21.8 wt %) at 600ºC with argon atmosphere up to 30 min [9]. Larger grains showed a better behavior due to the reduction of the grain boundary density and thus chromium depletion potential. Moreover, coatings on alloys have started to be investigated for this application. Indeed, MCrAlX coatings were applied on IN800H and 310SS and exposed to KCl-NaCl (55.47/34.42 wt%) at 700 °C under nitrogen atmosphere [10]. HVOF–NiCoCrAlYTa, pre-oxidized in air 24 h at 900 ºC, showed the best resistance with a corrosion rate of 190 μm/year, with a formation of a dense alumina layer. Abu-warda et al. studied HVOF-NiMoCrW and CoNiCrAlY coatings at 650 ºC for 360 h in presence of NaCl-KCl salts mixture in air. Their findings indicated that molybdenum has a beneficial effect in the corrosion resistance. They hypothesized that molybdenum presence inhibited the oxygen inward diffusion while favoring chromium fixation. They also consider that it avoids the formation of cracks in the chromium oxide layer by releasing internal stress when

* Corresponding author.
E-mail address: milambre@ucm.es (M. Lambrecht).

https://doi.org/10.1016/j.corsci.2022.110673
Received 20 April 2022; Received in revised form 14 September 2022; Accepted 15 September 2022
Available online 16 September 2022

forming micropores due to MoO_3 volatilization [11]. Hamdy et al. also confirmed that the presence of molybdenum in the alloys leads to a decrease of the chromium dissolution in chloride mixtures. These authors consider the formation of laves phases that acts as a barrier for chromium diffusion [5]. Finally, boronization on C276 and IN718 was tested in $MgCl_2$-KCl-NaCl (53/45/2 wt%) salt at 800 °C for 100 h under static conditions in an argon environment [12], and resulted in an average mass loss of 96% and 80 % for C276 and IN718 respectively. The aggressive behavior of Mg-based ternary salt comes from its corrosive impurities such as magnesium hydroxide (MgOHCl) coming from $MgCl_2$ hydrates decomposition by means of the reactions (1−4) [13–15].

$$MgCl_2.4\,H_2O \rightarrow MgOHCl + HCl + 3\,H_2O\ (129^{o}C) \quad (1)$$

$$MgCl_2.2\,H_2O \rightarrow aMgCl_2{\cdot}nH_2O + bMgOHCl + bHCl + (2\text{-}na\text{-}b)H_2O\ (1 \leq n \leq 2,\ a + b = 1)\ (167^{o}C) \quad (2)$$

$$MgCl_2{\cdot}nH_2O \rightarrow MgOHCl{\cdot}0{\cdot}3\,H_2O + HCl + (n\text{-}1{\cdot}3)H_2O\ (1 \leq n \leq 2)\ (203^{o}C) \quad (3)$$

$$MgOHCl{\cdot}0{\cdot}3\,H_2O \rightarrow MgOHCl + 0.3\,H_2O\ (235^{o}C) \quad (4)$$

Mortazavi et al. showed that a simple thermal dehydration process is useful for elimination of most hydrates, and suggested that the addition of Mg particles could protect alloys surfaces by interacting with oxyanions but should be only used below its melting point (649°C), for the cold leg of a CSP plant [16].

In this study, Ni-based IN617 have been immersed in MgNaK (53.9/24.3/21.8 wt%) chloride at 700°C under air atmosphere up to 24 h. The main objective of this investigation was to better understand the oxidation reactions occurring and to evaluate the stability of this alloy assuming a failure in an inertization process or a leak at real scale plant during operation.

2. Materials and methods

2.1. Computational modelling

Thermodynamic simulations have been carried out using Thermocalc. This software uses CALPHAD (CALculation of PHAse Diagrams) methodology for predicting thermodynamic, kinetic, and other properties of multicomponent material systems with the "Compound Energy Formalism" (CEF). The Gibbs energy of phases is computing with a better short range order accuracy, while it deals with not only the overall composition, but also its phase constituents such as neutral atoms, ions, or vacancies within the sublattices. The software was used to predict the main phases in the IN617 at the test temperature (700 °C) but covering a temperature range between 227 °C and 1227 °C. Thermodynamic simulations of IN617 under hydrated MgNaK chloride has been also performed by Thermocalc to be compared to the experimental results.

2.2. Corrosion testing

Inconel 617 (IN617) samples which composition can be found on Table 1 of 20 mm·10 mm·3 mm were grounded with abrasive 180 sandpaper and cleaned with distilled water followed by 5 min of sonication in ethanol. Prior to characterization, an unexposed sample was micro-etched using E407–07 ASTM standards, with a solution of 20 mL of HNO_3 and 80 mL of HCl, immersed up to 30 s. Then the sample was washed with distilled water, cleaned with ethanol, and dried.

$MgCl_2 0.6\ H_2O$, NaCl and KCl purchased from QUIMIPUR® were mixed to obtain the desired eutectic ternary mixture. Four identical samples were immersed in the salt, held in alumina crucibles, at 700°C, under air flow (50 mL/min) up to 24 h, in a Carbolite® electrical furnace. Each sample was tested used for a specific analysis, respectively three for the SEM-EDS, XRD, and Raman analysis, and one for the SEM-EDS cross analysis. A scheme of the experimental setup can be found on Fig. 1.

Microstructural characterizations of the samples and their corrosion layers were performed by Scanning Electron Microscopy JEOL® JSM-820 – Energy Dispersive Xray spectroscopy (SEM-EDX). The scanning electron microscope operated at 25 kV and with a backscattered electron detector, and EDX was used at a 10 mm working distance. For cross-sectional SEM analysis, the corroded samples were mounted in a phenolic resin (Buehler®). X-Ray diffraction (XRD) PANalytical® (X'Pert PRO MRD model) was used to identify the crystalline phases in the corrosion layer, with a copper target (Kα1 = 1.54056 Å y Kα2 = 1.54439 Å). The XRD operated at 45 kV and 40 mA, with a grazing incidence from 20° to 100°, and a timestep of 0.05° each 3 s. The Joint Committee on Powder Diffraction Standards (JCPDS) patterns were used for crystalline compounds identifications. Finally, Raman spectroscopy was used. Finally, Raman spectrometry was performed to identify spinel products, with an NT-MDT NTEGRA Spectra spectrometer equipped with a Solar TII MS5004i monochromator and an Andor iDUS DU-420 CCD detector. The excitation source is a solid-state laser of 532 nm wavelength and 22 mW power. Fig. 2.

3. Results and discussion

3.1. Computational modelling

Numerical simulations were performed to better understand the phases evolutions at high temperature during time. The simulation was performed on the calculation of the molar fraction of phases of IN617 at 700°C, in a window of 1000 K. The main phase at this temperature is austenitic Ni,Cr (FCC_A1), then $Ni_{10}Co_4(Cr,Mo)_{16}$ phase (sigma), $Cr_{20}Mo_3C_6$ carbides $M_{23}C_6$, TiC (FCC_A1#2), Cr_2NiP phase (M3PD0E), Cr5B3D8L and MNS.

Wu et al. tested IN617 [17] at 704°C for 65,600 h in helium atmosphere and the internal microstructure analysis confirmed the presence of Ti(C,N) (0.5–2 μm), $(Cr,Mo)_{23}C_6$ (cuboidal, sub-μm fine, plate-shaped agglomerates), Eta-M_6C (coarse + fine sub-μm plate-shaped), γ' (~200 nm, ~2 pct volume fraction) at intragrain, and Ti(C,N) (0.5–2 μm), $(Cr,Mo)_{23}C_6$ (2–10 μm) and Eta-M_6C (coarse) at grain boundaries.

Thermodynamic simulations of IN617 under hydrated MgNaK chloride has been taken from our previous review and can be compared to experimental results [3]. At equilibrium of the system at 700°C, the main oxidation products predicted are $CoCr_2O_4$, $MgMoO_4$ $MgAl_2O_4$ and $FeCr_2O_4$. Fig. 3.

Before testing, IN617 microstructure was analyzed with a micro-etching pre-treatment and a SEM capture can be seen on Fig. 4, with an EDS analysis for elemental scanning. In the intragrain, $M_{23}C_6$ carbide can be identified as $(Cr,Mo)_{23}C_6$. Moreover, a 21.8 μm Ti(C, N) grain is pointed out. Then, at grain boundaries, no strong variation occurred with the overall composition.

3.2. Surface analysis

Two SEM-EDS superficial analysis of IN617 after the 24 h immersion

Table 1
Chemical composition of IN617 (weight percent).

Element	Ni	Cr	Co	Mo	Al	Ti	Fe	Mn	Cu	Si	C	S	B
wt%	53.28	21.5	11.92	8.81	1.28	0.47	2.18	0.14	0.04	0.20	0.075	0.0003	0.0072

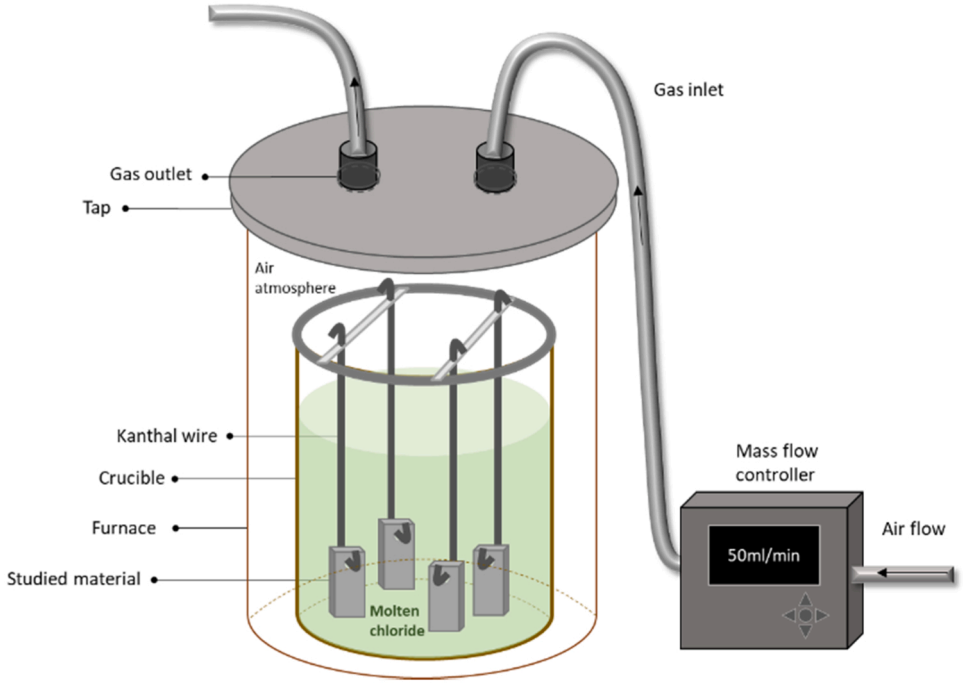

Fig. 1. Schematic representation of the corrosion test setup.

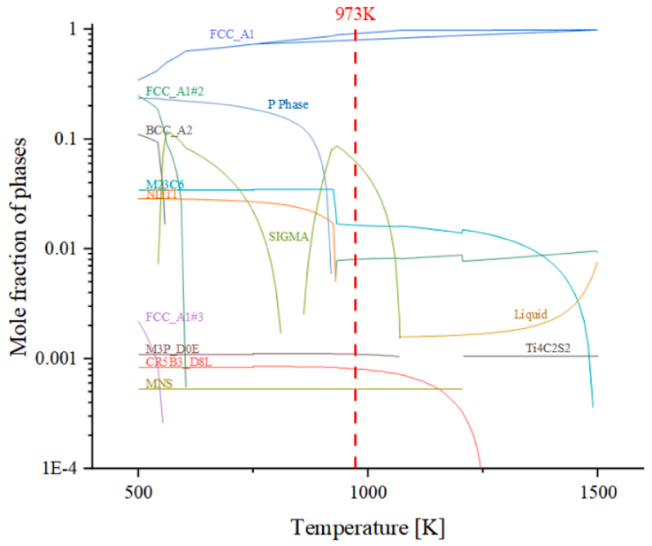

Fig. 2. Molar fraction of phases at equilibrium in IN617 at 700 °C (973 K).

were performed on different places of the sample (S1 and S2) and are showed on Figure. Elemental compositions of the analyses are referenced and the corresponding phases are proposed. It can be observed that salt-alloy interaction mainly leads to the formation of superficial multi-layers with a non-uniform relief. This surface appearance could be explained by spallation suffered by the samples along the experiment or the later washing step. Moreover, a bi-layer can be distinguished on S1 with a first formation of NiO, $(Mg,Cr)_2O_4$ [6,16,18], $MgAl_2O_4$ [7,11,16,19] and $(Co,Cr)_2O_4$ spinels transitions within the second layer and then, Al_2O_3 and formation on the outermost one. Indeed, NiO phase was not predicted by Thermocalc simulations but was confirmed in literature [9,20,21]. Furthermore, the analysis on S2 permits to identify $MgMoO_4$ spinel transition, Cr_2O_3 [11,20,22–24], NiO and precipitation of Ni,Mo-oxide. Fig. 5.

XRD analysis was performed on IN617 before and after 24 h immersion and their respective diffractograms are showed on Fig. 6a. MgO, Fe_3O_4, Fe_2O_3 and Cr_2O_3 were detected by 63.7 %, 19 %, 9.8 % and 7.5 % of magnitude respectively. Indeed, these phases stem from chromium, iron, and aluminum outward diffusion from the substrate. Then, magnesium oxide is precipitated by MgOHCl decomposition, following reaction (5) [25]. In parallel, Raman spectroscopy was used to better identify the potential spinels formed, as seen on Fig. 6b, to confirm to support and confirm the thermodynamic simulations. The Raman shifts correspond to magnesiochromite, magnesium aluminate and chromite spinels, with the presence of hematite. Indeed, these compounds formations can be explained by the reactions of α-Al_2O_3 and Cr_2O_3 stemming from aluminum and chromium outward diffusion, with MgO to form $MgAl_2O_4$ and $MgCr_2O_4$ respectively [16,26], following reactions (6−7). Plus, the precipitation of FeO and Cr_2O_3 at the surface, by iron and chromium reactions with oxygen anions, lead to the formation of $FeCr_2O_4$ following reactions (8−10). Indeed, this mechanisms need to be visualized by cross sections analysis due to the non-uniform aspect of the surface.

$$MgOHCl \rightarrow MgO + HCl \quad (415°C) \tag{5}$$

$$2Al^{3+} + 3O^{2-} \rightarrow Al_2O_3 \tag{6}$$

$$MgO + Al_2O_3 \rightarrow MgAl_2O_4 \tag{7}$$

$$Fe^{2+} + O^{2-} \rightarrow FeO \tag{8}$$

$$2Cr^{3+} + 3O^{2-} \rightarrow Cr_2O_3 \tag{9}$$

$$FeO + Cr_2O_3 \rightarrow FeCr_2O_4 + 2e^- \tag{10}$$

3.3. Transversal analysis

1D and 2D EDX mapping and linear scanning analysis were performed on the transversal section at different sites (T1, T2 and T3), to analyse the multilayer oxide formation. Indeed, the relative percentage of elements and spectrums of pointed sites can help to identify some complex phases, and an area mapping permits to visualize elements diffusion processes. First, T1, T2 and T3 show a mean of 230 μm, 220 μm

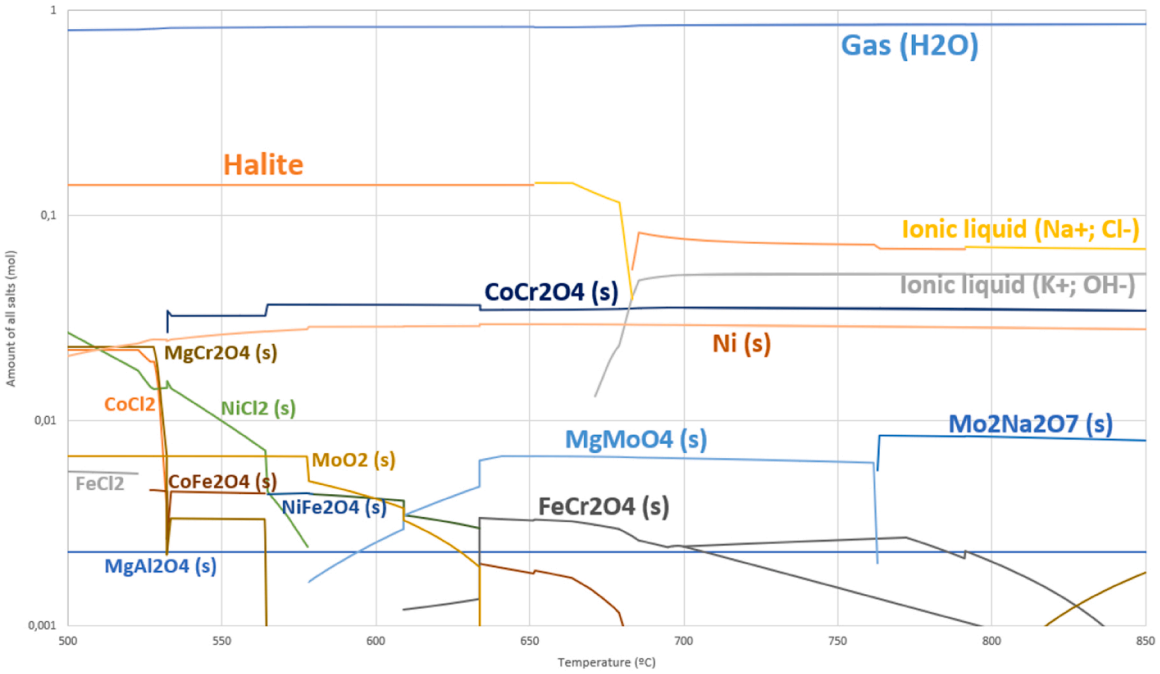

Fig. 3. Calculated phases present at the interface between IN617 and hydrated MgNaK chloride from 500 to 850CºC taken from ref [9].

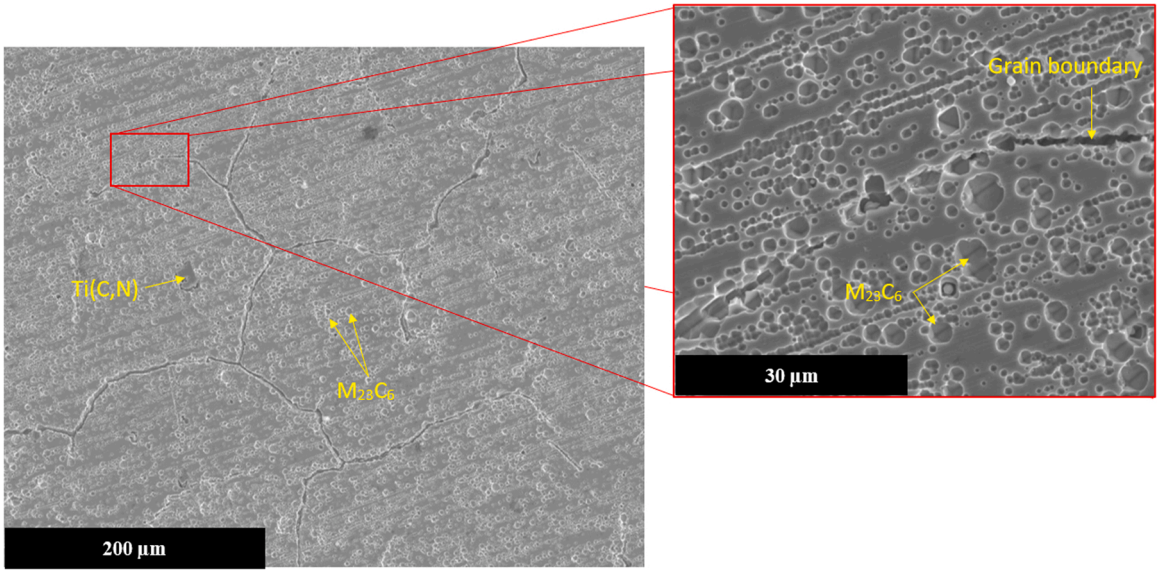

Fig. 4. IN617 initial microstructure micro-etched.

and 335 µm of oxidation scale respectively. For T1, an outermost layer of around 90 µm is mainly composed of magnesium, chromium and oxygen, and a thin layer of 5 µm on its top is composed of chromium and oxygen. The well known reaction of $CrCl_3$ with oxygen forming Cr_2O_3 and support from litterature [11,18,27–29] permits to identify these layers as $MgCr_2O_4$ and Cr_2O_3. Indeed, the formation of $MgCr_2O_4$ comes from the combined acid fluxing of MgO from MgOHCl decomposition and the basic fluxing from Cr_2O_3 and their synergistic dissolution, following reactions (11−14) [3,7,19].

$$2Cr^{3+} + 3O^{2-} \rightarrow Cr_2O_3 \quad (11)$$

$$Cr_2O_3 + O^{2-} \rightarrow 2CrO_2^- \quad (12)$$

$$MgO \rightarrow Mg^{2+} + O^{2-} \quad (13)$$

$$Mg^{2+} + 2CrO_2^- \rightarrow MgCr_2O_4 \quad (14)$$

Then, cracks in the middle and at the bottom of $MgCr_2O_4$ layer have been identified as iron chloride. Indeed, chloride oxydation of iron and its dissolution is a known issue as it generates electrons that lead to dioxyde electrolysis at salt-alloy interface and create oxyanions [27]. Plus, these instabilities could lead to spallation and explain the relief contrast on surface analysis. Furthermore, Al_2O_3 is present under $MgCr_2O_4$ as confirmed in the litterature [19,28–30]. At the innermost layer, a 25 µm Ni-Al- rich oxide is identified on top of a 3 µm Cr,Mo- rich corroded phase. Then, on Fig. 7b showing T2, the outermost layer presents $MgCr_2O_4$ on a 3 µm thin layer around a 60 µm MgO grain in a chromium-aluminum phase environment, identified as Cr_2O_3 and Al_2O_3, demonstrating a radial growth of $MgCr_2O_4$ at the expense of MgO (reaction 11–13). These phases coming indirectly from the salt interaction

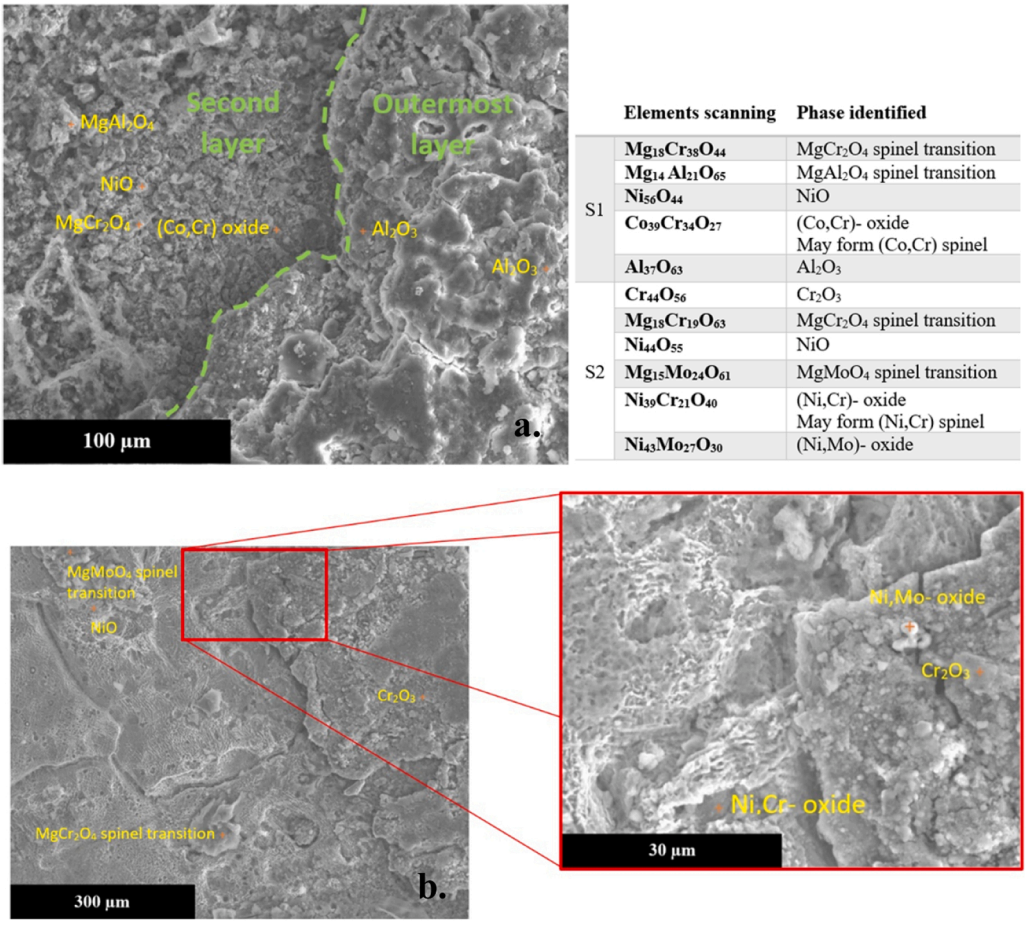

	Elements scanning	Phase identified
S1	$Mg_{18}Cr_{38}O_{44}$	$MgCr_2O_4$ spinel transition
	$Mg_{14}Al_{21}O_{65}$	$MgAl_2O_4$ spinel transition
	$Ni_{56}O_{44}$	NiO
	$Co_{39}Cr_{34}O_{27}$	(Co,Cr)- oxide May form (Co,Cr) spinel
	$Al_{37}O_{63}$	Al_2O_3
S2	$Cr_{44}O_{56}$	Cr_2O_3
	$Mg_{18}Cr_{19}O_{63}$	$MgCr_2O_4$ spinel transition
	$Ni_{44}O_{55}$	NiO
	$Mg_{15}Mo_{24}O_{61}$	$MgMoO_4$ spinel transition
	$Ni_{39}Cr_{21}O_{40}$	(Ni,Cr)- oxide May form (Ni,Cr) spinel
	$Ni_{43}Mo_{27}O_{30}$	(Ni,Mo)- oxide

Fig. 5. Superficial SEM analysis of IN617 after 24 h under MgNaK chlorides on a.S1 b.S2.

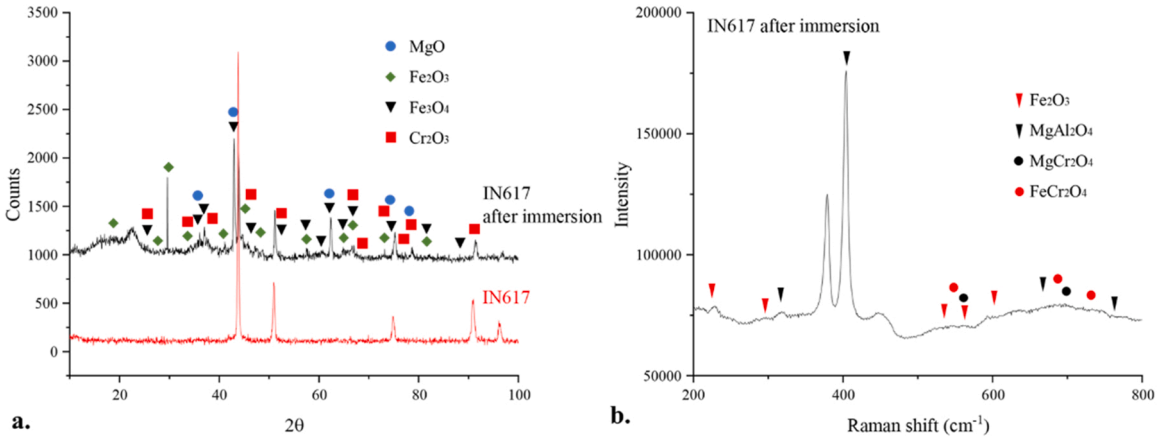

Fig. 6. a. XRD analysis of IN617 before and after immersion and b. Raman analysis after immersion, under MgNaK chloride at 700ºC in air atmosphere.

represent a layer of 100 µm, above a 17 µm Al_2O_3 phase, which interface is unstable, as separated by cracks. Aluminum outward diffusion has shown a strong role even though its concentration is low (1.28 at %) and is explained by its small atomic radius. Moreover, $MgAl_2O_4$ was also identified on the outermost layer, but no evidence was spotted of its growth over MgO grains, while it can be assumed that it forms in the same way as $MgCr_2O_4$, following reaction 15 [16]. A schematic representation of these spinels formation can be found on Fig. 8.

$$3Mg^{2+} + 4Al_2O_3 \rightarrow 2Al^{3+} + 3MgAl_2O_4 \quad (15)$$

Indeed, chlorine diffusion is limited by this area and oxides scales below are thus stemming from oxygen inward diffusion only. Then, nickel diffusion demonstrated a high chemical potential to the formation of several phases, such as NiO, Si,Ni- oxide and remaining Ni,Al- oxide on top of NiAl phase, limiting oxygen inward diffusion. Moreover, cobalt diffusion led to the formation of a cobalt-chromium-oxide, identifiable as $CoCr_2O_4$ spinel, but its presence is not as major as predicted by Thermocalc simulations. Nevertheless, cracks are still presents whereas those phases are non-uniform and the NiAl-oxide – NiAl interface seems unstable.

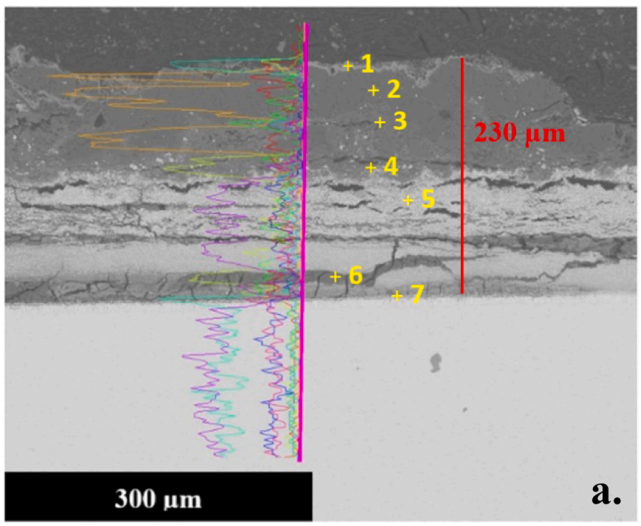

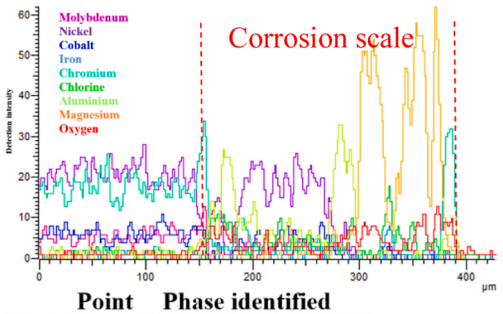

	Point	Phase identified
T1	1	Cr_2O_3
	2	MgO
	3	$FeCl_2$
	4	Al_2O_3
	5	Ni(Co,Al)- oxide
	6	Al,Cr- oxide
	7	Cr,Mo- rich phase

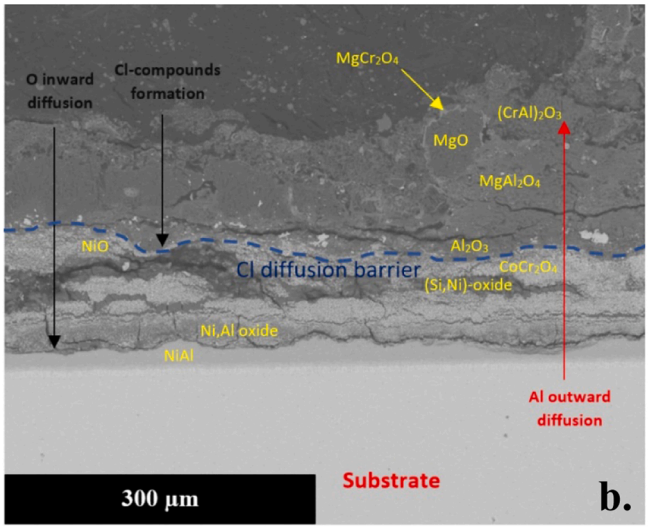

	Elements scanning	Phase identified
T2	$Mg_{16}Cr_{38}O_{44}$	$MgCr_2O_4$ spinel transition
	$Mg_{52}O_{48}$	MgO
	$Al_{39}Cr_{24}O_{32}$	(Cr,Al)- oxide; ($Cr_2O_3 - Al_2O_3$)
	$Mg_{12}Al_{29}O_{59}$	$MgAl_2O_4$
	$Al_{37}O_{63}$	Al_2O_3
	$Ni_{52}O_{48}$	NiO
	$Co_{16}Cr_{25}O_{59}$	$CoCr_2O_4$
	$Si_{56}Ni_{10}O_{23}$	(Si,Ni)- oxide
	$Al_{25}Ni_{24}O_{34}$	(Ni,Al)- oxide
	$Ni_{52}Al_{48}$	NiAl

Fig. 7. Linear and specific points SEM analysis of a transversal section of IN617 after 24 h immersed in MgNaK chloride, site a.T1 and b.T2.

EDS mapping on Fig. 9 shows the partition of the different relevant atoms present in a same area, at T3. Firstly, the chlorine-induced darker layer represents 200 µm, Interestingly, chlorine mapping permit to remark that diffusion lacks are only filled by magnesium and oxygen, and magnesium mapping is complementary with chromium, aluminum and iron ones as they are separated. It permits to identify several phases, such as magnesium oxide, chromium-aluminum oxide, aluminum oxide, and iron-chromium oxide. Moreover, chromium is present along magnesium grains and confirms the spectrum identification on T2, which shows the radial growth of $MgCr_2O_4$ over MgO. Furthermore, aluminum lower bright line delimits chromium, molybdenum and manganese outward diffusion and oxygen inward diffusion, acting as a barrier for these elements, and the aluminum second lower line seems acting as a barrier for nickel and cobalt outward diffusion. These two layers can be identified as NiAl and Al_2O_3 respectively.

4. Conclusions

IN617 were tested in MgNaK chloride at 700°C under air atmosphere for 24 h. Surface and cross analysis showed both a multilayered aspect of oxidation products. Indeed, several phases were identified on the outermost layers such as MgO, $Mg(Al,Cr)_2O_4$, Cr_2O_3, Al_2O_3, $FeCr_2O_4$, NiO, Ni-Mo-oxide, $MgMoO_4$ by SEM-EDX, XRD, and Raman analyses. Moreover, MgO grains deposition led to a radial growth of $MgCr_2O_4$ spinel and $MgAl_2O_4$ over MgO in a Cr_2O_3- and Al_2O_3- phase environment respectively, coming from chromium and aluminum outward diffusion. Furthermore, aluminum showed a key role in the oxidation process, as Al_2O_3 acted as a barrier to nickel and cobalt outward diffusion, and rich Ni-Al innermost layer reduced molybdenum, chromium and manganese outward diffusion, and blocked oxygen inward diffusion.

In parallel, Thermocalc simulations of IN617 in hydrated MgNaK chloride at high temperature showed relevant results predicting $CoCr_2O_4$, $MgMoO_4$ $MgAl_2O_4$ and $FeCr_2O_4$ which have been identified with respect to SEM-EDX analysis. Nevertheless, the simulated amount of phases is calculated at equilibrium and the results are not considering all the cascade-reactions of the corrosion process. Finally, the corrosion rate and structural instability of oxidation products observed in IN617 reveal that this alloy would not withstand a potential punctual failure in the inertization of a plant. Further research should consider oxygen leaks for real scale applications, with the need of an online atmosphere and corrosion monitoring systems, as presented in recent reviews [1,31], if chlorides are considered for real plant implementation.

CRediT authorship contribution statement

M. Lambrecht: Conceptualization, Validation, Writing – original draft, Writing – review & editing, Visualization **M.T. de Miguel:** Conceptualization, Validation, Investigation, Writing – review &

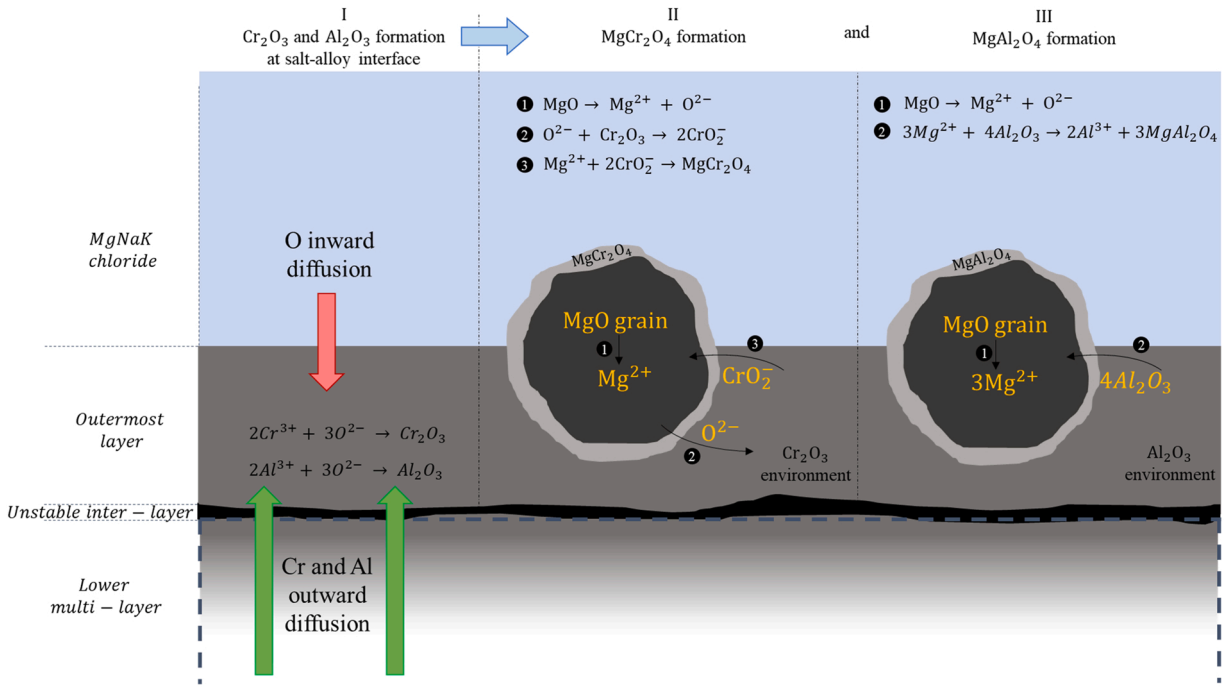

Fig. 8. Schematic representation of the radial growth of MgCr2O4 and MgAl2O4 over MgO grains at salt-alloy interface.

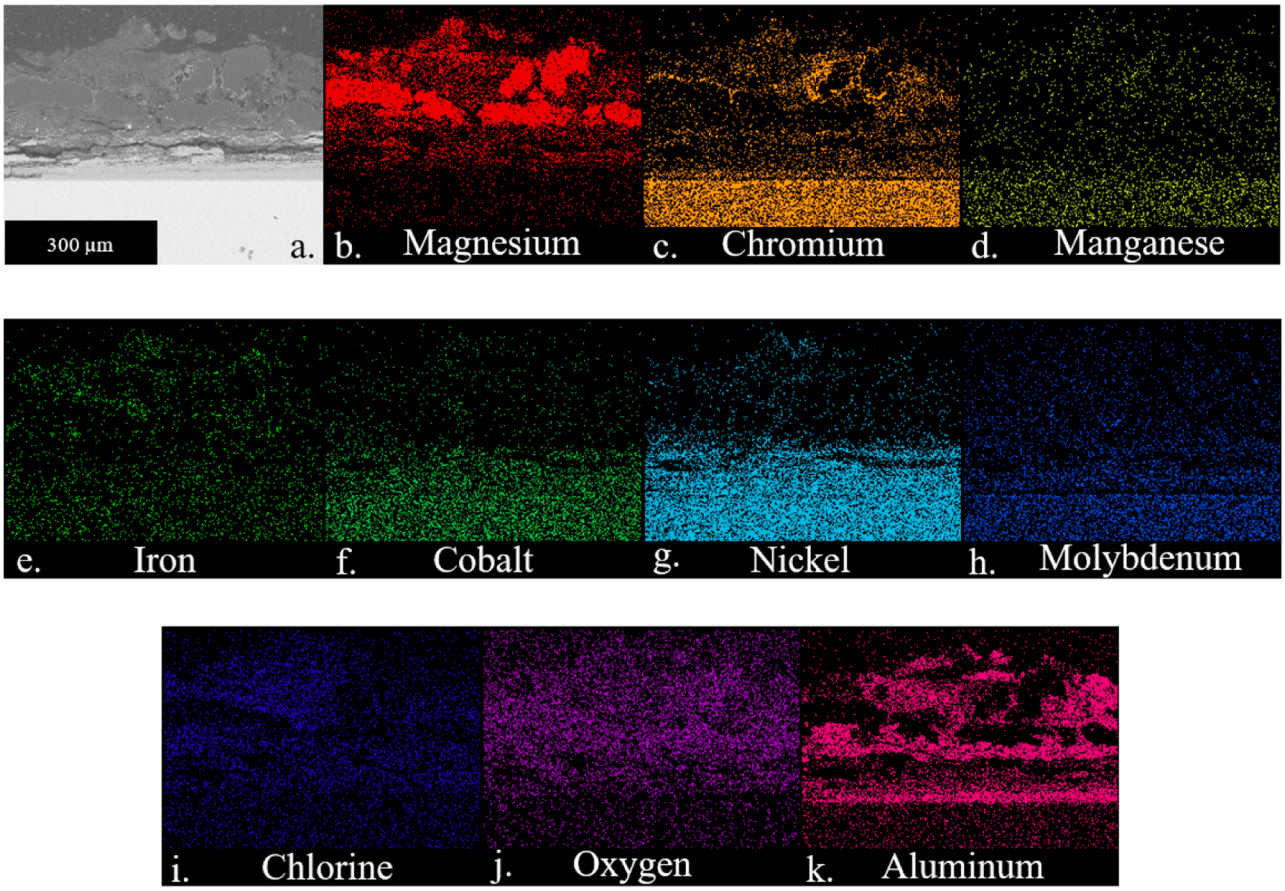

Fig. 9. EDS mapping of a transversal section of IN617 after 24 h immersion in MgNaK chloride, site T3.

editing, Visualization, Project administration **M.I. Lasanta:** Conceptualization, Methodology, Validation, Investigation, Project administration **G. García-Martín:** Resources, Writing – review & editing, Project administration **F.J. Pérez:** Conceptualization, Supervision, Funding acquisition.

Data Availability

The data that support the findings of this study are available from the corresponding author, Mickaël Lambrecht, upon reasonable request.

Acknowledgments

This work received funding from the Agencia Estatal de Investigación in the frame of the "Proyectos I + D + I 2020" program and under project reference number PID2020-115866RB-C22 (PID2020-115866RB-C22/AEI/10.13039/501100011033).

References

[1] C. Villada, et al., Engineering molten MgCl2–KCl–NaCl salt for high-temperature thermal energy storage: review on salt properties and corrosion control strategies, Sol. Energy Mater. Sol. Cells 232 (2021), 111344, https://doi.org/10.1016/j.solmat.2021.111344.
[2] D.W. Villada C, A. Bonk, T. Bauer, Simulation-assisted determination of the minimum melting temperature composition of MgCl2–KCl–NaCl salt mixture for next-generation molten salt thermal energy storage, Front. Energy Res (2022), https://doi.org/10.3389/fenrg.2022.809663.
[3] M. Lambrecht, et al., Past research and future strategies for molten chlorides application in concentrated solar power technology, Sol. Energy Mater. Sol. Cells (2022) **237**, https://doi.org/10.1016/j.solmat.2021.111557.
[4] W. Ding, A. Bonk, T. Bauer, Molten chloride salts for next generation CSP plants: selection of promising chloride salts & study on corrosion of alloys in molten chloride salts, AIP Conf. Proc. (2019) 10, https://doi.org/10.1063/1.5117729.
[5] E. Hamdy, J.N. Olovsjö, C. Geers, Perspectives on selected alloys in contact with eutectic melts for thermal storage: nitrates, carbonates and chlorides, Sol. Energy 224 (2021) 1210–1221, https://doi.org/10.1016/j.solener.2021.06.069.
[6] W. Ding, et al., Hot corrosion behavior of commercial alloys in thermal energy storage material of molten MgCl2/KCl/NaCl under inert atmosphere, Sol. Energy Mater. Sol. Cells 184 (2018) 22–30, https://doi.org/10.1016/j.solmat.2018.04.025.
[7] Q. Liu, et al., Ni-Mo-Cr alloy corrosion in molten NaCl-KCl-MgCl2 salt and vapour, Corros. Sci. 180 (2021), 109183, https://doi.org/10.1016/j.corsci.2020.109183.
[8] Q. Liu, et al., Corrosion behaviour of 316 stainless steel in NaCl-KCl-MgCl2 salt vapour at 700°C, Corros. Sci. 194 (2022), 109921, https://doi.org/10.1016/j.corsci.2021.109921.
[9] J. Feng, et al., Grain size effect on corrosion behavior of Inconel 625 film against molten MgCl2-NaCl-KCl salt, Corros. Sci. 197 (2022), 110097, https://doi.org/10.1016/j.corsci.2022.110097.
[10] J.C. Gomez-Vidal, Corrosion resistance of MCrAlX coatings in a molten chloride for thermal storage in concentrating solar power applications, Mater. Degrad. (2017) 9, https://doi.org/10.1038/s41529-017-0012-3.
[11] N. Abu-warda, et al., High temperature corrosion behavior of Ni and Co base HVOF coatings exposed to NaCl-KCl salt mixture, Surf. Coat. Technol. 418 (2021), 127277, https://doi.org/10.1016/j.surfcoat.2021.127277.
[12] B. D'Souza, et al., Corrosion behavior of boronized nickel-based alloys in the molten chloride Salt, Corros. Sci. 182 (2021), 109285, https://doi.org/10.1016/j.corsci.2021.109285.
[13] Q. Huang, et al., Thermal decomposition mechanisms of MgCl2·6H2O and MgCl2·H2O, J. Anal. Appl. Pyrolysis 91 (1) (2011) 159–164, https://doi.org/10.1016/j.jaap.2011.02.005.
[14] Smith and Veazey, Dehydration of magnesium chloride/patent. 1931: p. 12.
[15] Z. Zhang, et al., The dehydration of MgCl2·6H2O by inhibition of hydrolysis and conversion of hydrolysate, J. Anal. Appl. Pyrolysis 138 (2019) 114–119, https://doi.org/10.1016/j.jaap.2018.12.014.
[16] A. Mortazavi, et al., High-temperature corrosion of a nickel-based alloy in a molten chloride environment – the effect of thermal and chemical purifications, Sol. Energy Mater. Sol. Cells 236 (2022), https://doi.org/10.1016/j.solmat.2021.111542.
[17] Q. Wu, et al., Microstructure of long-term aged IN617 Ni-base superalloy, Metall. Mater. Trans. A 39 (2008) 2569–2585, https://doi.org/10.1007/s11661-008-9618-y.
[18] B. Liu, et al., Corrosion behavior of Ni-based alloys in molten NaCl-CaCl2-MgCl2 eutectic salt for concentrating solar power, Sol. Energy Mater. Sol. Cells 170 (2017) 77–86, https://doi.org/10.1016/j.solmat.2017.05.050.
[19] B. Grégoire, et al., Corrosion mechanisms of ferritic-martensitic P91 steel and Inconel 600 nickel-based alloy in molten chlorides. Part II: NaCl-KCl-MgCl2 ternary system, Sol. Energy Mater. Sol. Cells 216 (2020), https://doi.org/10.1016/j.solmat.2020.110675.
[20] S. Liu, et al., A comparative study on the high temperature corrosion of TP347H stainless steel, C22 alloy and laser-cladding C22 coating in molten chloride salts, Corros. Sci. 83 (2014) 396–408, https://doi.org/10.1016/j.corsci.2014.03.012.
[21] A. Ravi Shankar, A. Kanagasundar, U. Kamachi Mudali, Corrosion of nickel-containing alloys in molten LiCl-KCl medium, Corros. Sci. Sect. (2013), https://doi.org/10.5006/0627.
[22] T. Ishitsuka, K. Nose, Stability of protective oxide films in waste incineration environment—solubility measurement of oxides in molten chlorides, Corros. Sci. 44 (2) (2002) 247–263, https://doi.org/10.1016/S0010-938X(01)00059-2.
[23] A.V. Abramov, et al., Corrosion of austenitic stainless steels in chloride melts, Molten Salts Chem. Technol. (2014) 22, https://doi.org/10.1002/9781118448847.ch6e.
[24] M. Hofmeister, et al., Corrosion behaviour of stainless steels and a single crystal superalloy in a ternary LiCl–KCl–CsCl molten salt, Corros. Sci. 90 (2015) 46–53, https://doi.org/10.1016/j.corsci.2014.09.009.
[25] Q. Huang, et al., Thermal decomposition mechanisms of MgCl2·6H2O and MgCl2·H2O, J. Anal. Appl. Pyrolysis 91 (1) (2011) 159–164, https://doi.org/10.1016/j.jaap.2011.02.005.
[26] J.C. Gomez-Vidal, et al., Corrosion resistance of alumina-forming alloys against molten chlorides for energy production. I: pre-oxidation treatment and isothermal corrosion tests, Sol. Energy Mater. Sol. Cells 166 (2017) 222–233, https://doi.org/10.1016/j.solmat.2017.02.019.
[27] B. Grégoire, et al., Corrosion mechanisms of ferritic-martensitic P91 steel and Inconel 600 nickel-based alloy in molten chlorides. Part I: NaCl–KCl binary system, Sol. Energy Mater. Sol. Cells 215 (2020), 110659, https://doi.org/10.1016/j.solmat.2020.110659.
[28] A.G. Fernández, L.F. Cabeza, Corrosion evaluation of eutectic chloride molten salt for new generation of CSP plants. Part 2: materials screening performance, J. Energy Storage 29 (2020), https://doi.org/10.1016/j.est.2020.101381.
[29] J.C. Gomez-Vidal, et al., Corrosion resistance of alumina forming alloys against molten chlorides for energy production. II: electrochemical impedance spectroscopy under thermal cycling conditions, Sol. Energy Mater. Sol. Cells 166 (2017) 234–245, https://doi.org/10.1016/j.solmat.2017.03.025.
[30] W. Ding, et al., Molten chloride salts for next generation concentrated solar power plants: mitigation strategies against corrosion of structural materials, Sol. Energy Mater. Sol. Cells 193 (2019) 298–313, https://doi.org/10.1016/j.solmat.2018.12.020.
[31] T.C. Ong, et al., Review of the solubility, monitoring, and purification of impurities in molten salts for energy storage in concentrated solar power plants, Renew. Sustain. Energy Rev. 131 (2020), https://doi.org/10.1016/j.rser.2020.110006.